ChemPubSoc Europe

DOI: 10.1002/celc.201902068

CHEMELECTROCHEM Articles

VIP *Very Important Paper*

# Current-Induced Ion Concentration Polarization at a Perfect Ion-Exchange Patch in an Infinite Insulating Wall

Mykola P. Bondarenko,[a] Merlin L. Bruening,*[b, c] and Andriy E. Yaroshchuk[d, e]

An invited contribution to the *Richard M. Crooks* Festschrift

This research examines, theoretically, the ion concentration polarization, ion fluxes, and electrostatic fields near an ion-exchange patch in the wall of an electrified fluidic channel. These phenomena are important in related microfluidic ion-preconcentration systems. Under an electric field, counter ions enter the ion-exchange patch at one side and leave at the other, with salt depletion occurring near the entrance and accumulation near the exit. The high patch conductivity and the concentration profiles lead to local electric field perturbations that may facilitate preconcentration. This study includes analytical expressions of ion concentrations and electrochemical potentials at small to moderate electric fields, as well as numerical simulations. Additionally, a simple matrix of polynomial coefficients (obtained via fitting of numerical data) enables analytical calculation of the two-dimensional concentration profiles at all electric fields within the range investigated in the numerical simulations. This is possible because a single dimensionless parameter controls this problem.

## 1. Introduction

This manuscript mathematically investigates the ion concentration polarization that occurs upon application of a potential difference across a microchannel that spans an ion-exchange patch. Such systems provide perhaps the simplest method for ion preconcentration in microchannels, and the important point of this work is to demonstrate the pronounced local depletion/enrichment phenomena that occur close to ion-exchange patches that behave like floating electrodes (in the sense that the net electric current through them is zero).

The Crooks group was among the first to demonstrate ion preconcentration that results from depletion zones adjacent to nanopores or ion-exchange membranes.[1] They inserted a nanoporous polyester membrane between two poly(dimethylsiloxane) channels and applied a potential between the channels (Figure 1A and 1B). DNA accumulated in the channel above the membrane. One possible explanation for the accumulation is that the nanoporous membrane is negatively charged and behaves as a modestly selective cation-exchange membrane. In such cases, supporting salt depletion will occur on the anodic side of the membrane, whereas accumulation will occur on the cathodic side. This leads to high local electric fields, and when combined with electroosmotic flow, such fields should lead to DNA accumulation.

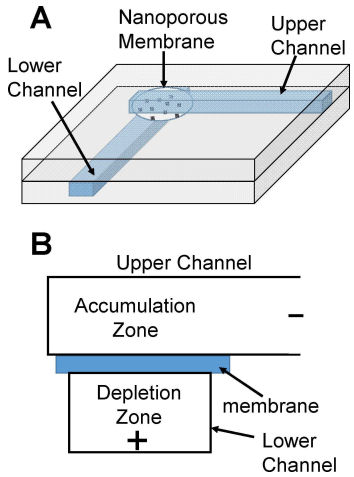


**Figure 1.** Scheme of one of the earliest devices for preconcentration in microfluidic devices. A) Three-dimensional view. B) Vertical cross section of the device.

The electrodialysis community has known about accumulation and depletion zones since the 1950s.[2–3] Such membranes contain a high concentration of net fixed charge and are important in fuel cells and electrodialysis.[4–5] Upon application of a current across an ion-exchange membrane, the difference in ion electromigration flux components in the solution and the membrane leads to ion depletion adjacent to one side of the membrane and ion accumulation adjacent to the other side.[2,6] Considering the cation-exchange membrane (CEM) in Figure 2,

[a] *Prof. M. P. Bondarenko*
*Institute of Bio-Colloid Chemistry*
*National Academy of Sciences of Ukraine*
*Vernadskiy ave.42, 03142, Kyiv, Ukraine*
[b] *Prof. M. L. Bruening*
*Department of Chemical and Biomolecular Engineering*
*University of Notre Dame*
*Notre Dame, Indiana 46556, United States*
*E-mail: mbruenin@nd.edu*
[c] *Prof. M. L. Bruening*
*Department of Chemistry and Biochemistry*
*University of Notre Dame*
*Notre Dame, Indiana 46556, United States*
[d] *Prof. A. E. Yaroshchuk*
*ICREA, pg. L.Companys 23, 08010 Barcelona, Spain*
[e] *Prof. A. E. Yaroshchuk*
*Department of Chemical Engineering*
*Polytechnic University of Catalonia*
*av. Diagonal 647, 08028 Barcelona, Spain*

Supporting information for this article is available on the WWW under https://doi.org/10.1002/celc.201902068

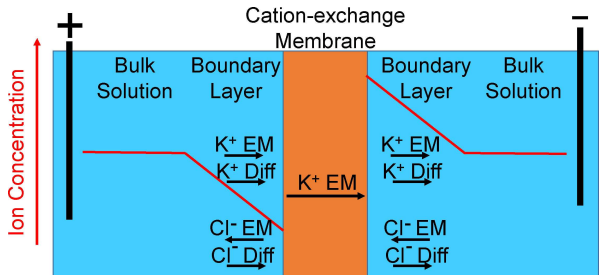


**Figure 2.** Scheme of concentration polarization during electrodialysis across an ion-exchange membrane. The arrows show qualitative electromigration (EM) and diffusion (Diff) flux components for $K^+$ and $Cl^-$ in a solution containing KCl. The drawing assumes negligible ion diffusion in the ion-exchange membrane and complete anion exclusion.

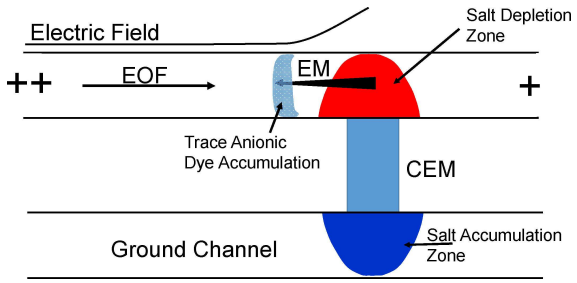


**Figure 3.** Scheme of preconcentration during application of a potential between two channels connected by a cation-exchange membrane (CEM). Depletion of dominant ions above the channel leads to a large electric field in this area. Trace anions accumulate near this region because to the left of the dye accumulation region electroosmotic flow (EOF) is greater than the dye electromigration, but the dye EM increases with the electric field strength and eventually offsets the EOF to create accumulation.

if the solution contains KCl as the dominant salt, the $K^+$ and $Cl^-$ ions each carry about half of the current in the solution. However, inside the CEM, $K^+$ carries essentially all of the current. Thus, the electromigration of $K^+$ to the membrane from solution on the left is less than the electromigration flux of $K^+$ away from this interface into the membrane. Similarly, in the solution on the left side of the membrane the electromigration flux of $Cl^-$ away (to the left) from the membrane is higher than the flux of $Cl^-$ (to the left) through the membrane because anions carry little current in the CEM. These phenomena deplete the concentrations of both cations and anions near the left side of the membrane. At underlimiting currents with negligible convective flow and a thick membrane, the sum of diffusive and electromigration flux components of either cations or anions in the boundary layer is equal to their electromigration fluxes through the CEM. In a related manner, the difference in the fraction of current that cations and anions carry in the membrane and in the solution to the right of the membrane leads to an accumulation region adjacent to the right side of the membrane (Figure 2). Note that to some extent these accumulation and depletion regions will appear in any case when cations and anions carry different fractions of current in the solution and in the membrane, i.e. when their transference numbers are different in the solution and the membrane.[3] This can occur in charged nanopores, which function as ion-exchange membranes at low ionic strength.

After the initial Crooks paper, many groups developed ion preconcentration using ion- exchange media, including nanopores, between channels in a T-junction configuration (Figure 3).[7] These devices also exploit the combination of flow with depletion and accumulation regions that exist near the surfaces of ion-exchange media during current flow.[8–10] Typically, flow brings ions toward the junction, and they accumulate near regions where their electrophoretic flux component offsets their convective flux component. Wang and coworkers reported as much as a million-fold preconcentration factor for proteins.[10] Our recent computer simulations suggest that ion accumulation near a related nanoporous interface can occur with order of magnitude selectivity for ions with different (but relatively close) mobilities.[11]

In research to simplify the construction of preconcentration devices, the Crooks group expanded on their prior expertise with bipolar electrodes[12–13] to create enrichment zones with only a single channel that spans a bipolar electrode (Figure 4A).[14–18] Because of the potential profile in the solution above the electrode, the electrode minus solution potential drop is more negative at the right side of the electrode than at the left side. Thus, (at sufficiently high electric fields in solution) the right side of the electrode behaves as a cathode and the left side as an anode, and current flows through the electrode (Figure 4B). Importantly, the bipolar electrode provides a low-resistance pathway for current flow, so the electric field in the solution above the bipolar electrode is much smaller than in surrounding areas. This results in minimal electromigration above the electrode, which leads to depletion of chloride ions (the buffer is Tris-HCl) because EOF moves them away from this region to the left. Moreover, hydroxide generated at the cathode neutralizes Tris-$H^+$ ions to deplete them above and to the right of the bipolar electrode. The ion depletion to the right

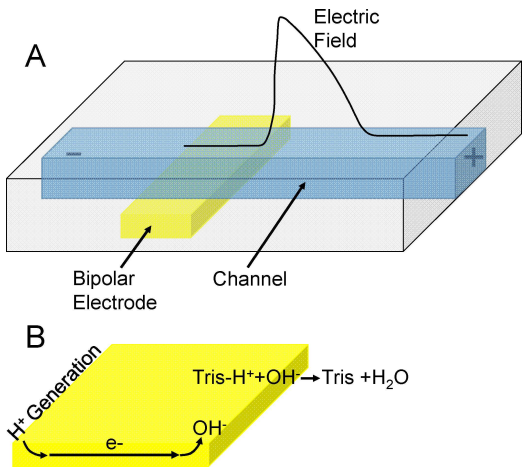


**Figure 4.** A) Scheme of a channel that spans a bipolar electrode to create a depletion region and high electric field to the right of the electrode. B) Diagram of the bipolar electrode showing cathodic and anodic reactions. Generated hydroxide ions deplete Tris-$H^+$ to deplete cations near and to the right of the electrode.[14]

side of the electrode creates a large electric field that allows accumulation of anionic dyes at a point near where their electrophoretic and electroosmotic velocities essentially offset. Simulations in both Tris and carbonate buffers show that the system is complicated,[14] but the principles of ion depletion and accumulation in regions where electrophoretic and electroosmotic velocities approximately counteract are vital to the accumulation.

Following the simple single-channel preconcentration with bipolar electrodes, Han and coworkers demonstrated trace analyte accumulation in a single channel containing an ion-exchange patch (Figure 5).[19] Other research employed paper-based fluidic devices containing Nafion plugs or membranes[20–22] Devices with a channel containing a Nafion patch resemble those with bipolar electrodes. The high counter ion concentration in the patch leads to a high conductivity, so the patch may carry a significant fraction of the total current in this region. Moreover, at the region where cations enter the patch, ion depletion occurs and, in the region where cations exit the patch, ions accumulate. The principle is related to that shown in Figure 2. Due to perm-selectivity,[23] in a cation-exchange patch cations will carry most of the current. Although the system resembles a channel containing a bipolar electrode, the ion-exchange patch is easier to model because of the absence of electrode reactions.

This work aims to mathematically assess the salt depletion/enrichment phenomena that ultimately make possible co-ionic-species accumulation in microfluidic channels that span ion-exchange patches. A number of studies mathematically simulated the ion concentration polarization that occurs when using T-junctions such as those in Figure 3, and such simulations are complex as they may include nonlinear electrokinetic flow near the junction.[24–27] Crooks and Tallarek simulated and measured electric fields near channels containing bipolar electrodes.[15] As noted, the system with an ion-exchange patch is simpler than the bipolar-electrode system because there are no electrode reactions. We previously showed that the assumption of a highly conductive patch (no change in electrochemical potentials of counter ions along the patch) and relatively low electric fields in solution leads to expected accumulation and depletion regions where current enters and leaves the patch.[28] However, such a limiting case does not adequately describe strongly-polarized systems that can give high levels of preconcentration. This work develops methods to examine higher electric fields under relatively simple conditions, and also examines local ion fluxes and electric fields.

The system we consider is qualitatively related to the above preconcentration devices based on ion concentration polarization. We do not pretend to describe practical systems adequately, rather we demonstrate in what way a combination of analytical and numerical approaches enables one to carry out a complete parametric study of a simplest non-trivial system and present the results in a compact and exhaustive way. Meanwhile, one of the most serious issues with many published numerical analyses is the presentation of results. Usually, researchers select a few parameter combinations so parametric studies are not exhaustive (or sometimes even representative). Finally, we draw attention to some perils of "fully numerical" analysis.

Ion-exchange patches may not only be simpler to model, but they also may perform better than T-junctions in sample preconcentration. Indeed, in T-junction configurations, different current densities in the branches of the principal channel (occurring due to some current shunting into the side channel) lead to hydrostatic-pressure gradients within both principal branches (to make the convective flows there equal). This can give rise to Taylor dispersion and impair sample focusing. Close to current-polarized ion-exchange patches, there are also some perturbations of electroosmotic flow, but they do not extend far from the patch (provided that the patch width is much smaller than the channel length).

Moreover, ion-exchange patches give rise to a redistribution of salt close to the patch whereas in T-junction configurations (at noticeable current deviations into the ion exchange-filled branch) there is predominantly either depletion or enrichment (depending on the sign of deviating current). In the situation of redistribution, appropriate co-ionic species accumulate at the front edge of the buffer-depletion zone while they are "swept" away from the buffer-enrichment zone due to the reduced electrical flux component (and relatively stronger convective component) there. This can lead to sharper preconcentration profiles. This aspect has not, yet, been pointed out in the T-junction research. Moreover, it has never been clearly stated before that the local ion concentration polarization pattern stems not necessarily from a net electric current flowing through the ion exchange-containing branch but primarily due to the current "entering" and "leaving" at different parts of the ion-exchange region.

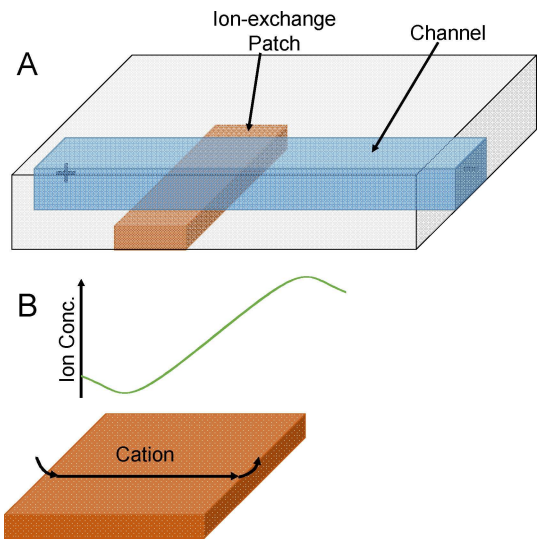


**Figure 5.** A) Scheme of a channel that spans an ion-exchange patch. B) Diagram of the current that flows through a cation-exchange patch to create depletion and accumulation regions.

## 2. Theory

### 2.1. Problem Statement (Fluxes and Boundary Conditions)

In this study, we consider only solutions of single salts. For simplicity, we assume local electroneutrality and neglect convection. The Nernst-Planck equations describe the ion flux vectors, $\vec{j}_i$ [Eq. (1)]:

$$-\vec{j}_i = D_i \cdot \nu_i \cdot \left(\vec{\nabla}\tilde{c} + \frac{ZiF}{RT}\tilde{c}\vec{\nabla}\tilde{\varphi}\right) \tag{1}$$

where $D_i$ is the ion diffusion coefficient, $\nu_i$ is the ion stoichiometric coefficient in the salt, $\tilde{c}$ is the salt concentration, $Z_i$ is the ion charge, $\tilde{\varphi}$ is the electrostatic potential, and $i = 1$ *or* 2. The symbols $F$, $R$, and $T$ represent Faraday's constant, the gas constant, and temperature, respectively. Equation (1) assumes that due to local electroneutrality [Eq. (2)]:

$$\nu_i\tilde{c} = \tilde{c}_i \tag{2}$$

where $\tilde{c}_i$ is the concentration of ion $i$. Under steady-state conditions, the ion fluxes must be conservative, so their divergences have to be zero. Taking this into account as well as the electroneutrality of the salt and combining the equations for the two ions leads to Equations (3) and (4); see the Supporting Information section S1 for details:

$$\nabla^2\tilde{c} = 0 \tag{3}$$

$$\tilde{c}\nabla^2\tilde{\varphi} + \left(\vec{\nabla}\tilde{c}\cdot\vec{\nabla}\tilde{\varphi}\right) = 0 \tag{4}$$

where the second term in Eq. (4) is the scalar product of gradients of salt concentration and electrostatic potential.

We consider the steady-state distribution of salt concentration and electrostatic potential in the vicinity of a perfect ion-exchange patch in an infinite insulating wall (see Figure 6). The patch extends infinitely in both $z$-directions. For convenience, we scale the $x$ and $y$ coordinates on the half-width of the patch, $l$, to create dimensionless variables. Additionally, we introduce a dimensionless electrostatic potential $\varphi \equiv F\tilde{\varphi}/RT$. Finally, we scale the salt concentration by its bulk value (i.e., $c \equiv \tilde{c}/\tilde{c}_0$, where $\tilde{c}_0$ is the bulk concentration). One can rewrite Equations (3) and (4), in terms of these dimensionless variables to give Equations (5) and (6):

$$\nabla^2 c = 0 \tag{5}$$

$$c\cdot\nabla^2\varphi + \left(\vec{\nabla}c\cdot\vec{\nabla}\varphi\right) = 0 \tag{6}$$

Our statement of the surface boundary conditions (see Figure 6) required to solve these equations begins with the assumption that the whole wall (including the patch) is impermeable to co-ions (termed ion "2"), so their flux in the $y$-direction must be zero everywhere at $y = 0$. (The sign of the charge on the co-ions is equal to the sign of the fixed charge in the ion-exchange patch.) Based on the $y$-direction Nernst-Planck equation, this leads to Equation (7):

$$\frac{\partial c(x,0)}{\partial y} + Z_2 c(x,0)\cdot\frac{\partial\varphi(x,0)}{\partial y} = 0 \tag{7}$$

Outside the patch, the wall is also impermeable to counter ions (termed ion "1", the sign of the counter ion charge is opposite to that of the fixed charge in the patch) so:

$$\frac{\partial c(x,0)}{\partial y} + Z_1 c(x,0)\cdot\frac{\partial\varphi(x,0)}{\partial y} = 0 \;@\; x < -1 \;\cup x > 1 \tag{8}$$

To satisfy both Equations (7) and (8), we use Equation (9):

$$\frac{\partial c(x,0)}{\partial y} = 0 \;\; \frac{\partial\varphi(x,0)}{\partial y} = 0 \;@\; x < -1 \;\cup x > 1 \tag{9}$$

Further, we assume that the electrochemical potential of counter ions is constant (albeit generally unknown) at the patch surface. This assumption implies that the ion-exchange patch is infinitely conducting so that there is no change in the electrochemical potential of counter ions in the patch in the $x$-direction. Based on the definition of the electrochemical potential, $\bar{\mu}_1$, this assumption leads to Equation (19); see the Supporting Information, section S2:

$$\frac{\partial\bar{\mu}_1(x,0)}{\partial x} \equiv \frac{\partial c(x,0)}{\partial x} + Z_1 c(x,0)\cdot\frac{\partial\varphi(x,0)}{\partial x} = 0 \;@ -1 < x < 1 \tag{10}$$

Using the condition of patch impermeability to co-ions, Eq. (7), one can substitute for the normal derivative of electrical potential in the expression for the normal gradient of electrochemical potential of counter ions. This leads to Eq. (11), which shows that the normal derivative of the dimensionless counter ion electrochemical potential is proportional to the normal derivative of dimensionless salt concentration.

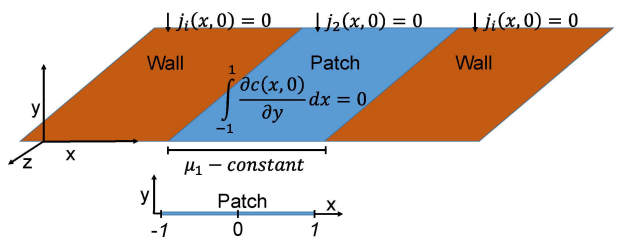


**Figure 6.** Scheme of an ~~ion-patch~~ in a channel wall showing coordinates and surface boundary conditions. The patch extends infinitely in both z-directions.

$$\frac{\partial \bar{\mu}_1(x,0)}{\partial y} \equiv \frac{\partial c(x,0)}{\partial y} + Z_1 c(x,0) \cdot \frac{\partial \varphi(x,0)}{\partial y} = \left(1 - \frac{Z_1}{Z_2}\right) \cdot \frac{\partial c(x,0)}{\partial y} \quad @ \quad -1 < x < 1 \tag{11}$$

For a patch that is impermeable to co-ions, the electric current flowing into and out of the patch stems exclusively from counter ions. Therefore, from the condition of zero net current into the patch (due to the patch behaving as a floating electrode), the integral of normal counter ion flux into the patch must be zero. Because normal counter ion flux is proportional to the normal derivative of its electrochemical potential, based on Eq. (11) the integral of the normal concentration derivative over the patch must also be zero [Eq. (12)].

$$\int_{-1}^{1} \frac{\partial c(x,0)}{\partial y} dx = 0 \tag{12}$$

Far away from the patch, there is a homogeneous electric field parallel to the wall and a constant salt concentration [Eqs. (13)–(15)]:

$$\varphi(x,y) \underset{x\to\pm\infty, y\to\infty}{\to} -2\lambda x \tag{13}$$

$$c(x,y) \underset{x\to\pm\infty, y\to\infty}{\to} 1 \tag{14}$$

$$\lambda \equiv \frac{FE_0 l}{2RT} \tag{15}$$

These boundary conditions complete the statement of the problem. In this study, we consider positive counter ions, so a positive electric field (positive $\lambda$) results in movement of counter ions from left to right and co-ions from right to left. Notably, the strength of the external perturbation (electric field) enters the problem [in Eq. (13)] only via $\lambda$, which is the single essential parameter. The remaining equations and boundary conditions depend additionally solely on the valence type of the electrolyte. Of course, the ion fluxes also depend on the ion diffusion coefficients, but remarkably these coefficients do not affect the distributions of dimensionless concentration and dimensionless electrostatic potential.

### 2.2. Representation of Concentration Distribution via its Normal Derivative at the Patch

Because concentration satisfies the Laplace equation, in this section we will represent the two-dimensional salt-concentration distributions (for each dimensionless voltage drop) in terms of a single function of one variable defined within a finite range. We show below that this function enables compact presentation of results and development of a procedure for the approximation of numerical data with a set of analytical functions.

The dimensionless salt concentration satisfies the Laplace equation [see Eq. (5)]. Direct differentiation and substitution show that any function of the form in Equation (16):

$$G(x,y) = \int_{-1}^{1} f(s) \cdot ln\left(\sqrt{(x-s)^2 + y^2}\right) ds \tag{16}$$

fulfills the Laplace equation (see the supporting information, section S3). Via differentiation under the integral we obtain Equation (17):

$$\frac{\partial G}{\partial y} = \int_{-1}^{1} f(s) \cdot \frac{y}{(x-s)^2 + y^2} ds \tag{17}$$

Importantly, $G(x,y)$ has a zero $y$-derivative at the wall outside the patch, which fulfills the concentration boundary condition in Equation (9). At very small values of y, the factor $\frac{y}{(x-s)^2+y^2}$ behaves as a delta-function of $(x-s)$: it tends to infinity at $x \to s$ and is vanishingly small elsewhere. Thus, as $y$ approaches zero only a very small part of the integration range (in close proximity to $s = x$) where $f(s) \approx f(x)$ contributes to the integral [Eq. (18)]. Accordingly,

$$\frac{\partial G}{\partial y} \approx f(x) \cdot \int_{-1}^{1} \frac{y}{(x-s)^2 + y^2} ds \equiv f(x) \cdot \left(atan\left(\frac{1-x}{y}\right) + atan\left(\frac{1+x}{y}\right)\right) \underset{y\to 0}{\to} \pi f(x) \tag{18}$$

Therefore, we get Equation (19):

$$f(s) = \frac{1}{\pi} \cdot \left.\frac{\partial G(s,y)}{\partial y}\right|_{y\to 0} \tag{19}$$

and one can present the distribution of perturbation of dimensionless concentration via its normal derivative at the patch as:

$$\delta c(x,y) = \frac{1}{\pi} \cdot \int_{-1}^{1} \frac{\partial \delta c(s,0)}{\partial y} \cdot ln\left(\sqrt{(x-s)^2 + y^2}\right) ds \tag{20}$$

where we have denoted

$$\delta c(x,y) \equiv c(x,y) - 1 \tag{21}$$

Note that both $\delta c(x,y)$ and $c(x,y)$ [Eq. (21)] satisfy the Laplace equation and the concentration boundary condition in Eq. (9) because their derivatives are equal. Addition of a 1 to the function in Eq. (20) will still give a function that solves the Laplace equation and have zero derivative outside the patch. However, conveniently the value of $\delta c(x,y)$ goes to zero at large $x$ and $y$, whereas $c(x,y)$ goes to 1.

Due to the zero net flux of counter ions through the patch [see also Eq. (12)]:

$$\int_{-1}^{1} \frac{\partial \delta c(s,0)}{\partial y} ds = 0 \tag{22}$$

One can take the integral in Eq. (20) by parts to yield Eq. (23)

$$\delta c(x,y) = \frac{1}{\pi} \int_{-1}^{1} F(s) \cdot \frac{x-s}{(x-s)^2 + y^2} ds \tag{23}$$

where

$$F(s) \equiv \int_{-1}^{s} \frac{\partial \delta c(s',0)}{\partial y} ds' \tag{24}$$

In the integration by parts, we use the definitions of Eq. (24) and Eq. (22) to obtain Eq. (25):

$$F(-1) = F(1) = 0 \tag{25}$$

$F(s)$ is proportional to the cumulative counter-ion flux (and electric current) occurring through the part of the patch extending from its left edge ("entrance") to the observation point (the upper limit of integration). Its value at the "exit" edge ($x = 1$) is zero because there must be no net current through the "floating" patch.

Thus, for a given $\lambda$ the solution of the concentration-distribution problem reduces to finding a function of one variable, $F(s)$, and then inserting this function into Eq. (23). Since many relevant dependences can be generated once this function is found, we will refer to it is a generating function. Finding $F(s)$ requires solving for an additional variable coupled to the salt concentration in this problem. In our numerical calculations, this is the dimensionless electrostatic potential. As we will see below, for analytical solutions at low fields it is more convenient to use the electrochemical potential of co-ions as the additional variable. This convenience stems from the extremely simple boundary condition at the wall, zero co-ion normal flux everywhere.

### 2.3. Linear Approximation

This section develops an expression for the concentration profile at weak electric fields that produce small perturbations in concentration gradients. This approximate expression allows us to assess the accuracy of numerical computations because under small fields analytical expressions are more accurate than numerical methods due to the finite numerical mesh size. At weak fields, one can neglect the second term in Eq. (4) because it is proportional to the product of gradients of concentration and electrostatic potential, both of which are proportional to the applied field [see below, Eq. (35)]. Thus, this second term is of higher order with respect to the field than the first term. Accordingly, at weak electric fields we obtain Laplace equations for both concentration and electrostatic potential and can express them through their normal derivatives at the patch surface as in Eq. (20). Moreover, presented in this way, the functions automatically satisfy the condition of zero normal derivative outside the patch [Eq. (9)]. At low fields, the variation of concentration along the patch in Eq. (7) can be neglected ( $c(x,0) \approx 1$), which means that this condition is formulated for a linear combination of normal gradients of concentration and electrostatic potential. Such a condition can only be satisfied at any point of the wall when the concentration and potential distributions are similar functions that differ only by a constant factor and a linear function of coordinate (which identically satisfies the Laplace equation). To obtain the appropriate concentrations and electric fields at negative and positive infinity [Eqs. (13) and (14)] we seek solutions in these forms [Eqs. (26) and (27)]:

$$c(x,y) = 1 + B_c \cdot g_0(x,y);\ \ \delta c(x,y) = B_c \cdot g_0(x,y) \tag{26}$$

$$\varphi(x,y) = -2\lambda x + B_\varphi \cdot g_0(x,y);\ \ \delta\varphi(x,y) = B_\varphi \cdot g_0(x,y) \tag{27}$$

where $g_0(x,y)$ is a function that fulfills the Laplace equation and goes to zero at large values of $x$ and $y$. The conditions of zero normal flux of co-ions and constant electrochemical potential of counter ions at the patch will dictate the values of the constants $B_c$, $B_\varphi$.

In the linear approximation the variation of concentration along the patch surface is negligible compared to the bulk concentration so $c(x,0) \approx 1$. Thus, Eq. (7) becomes Equation (28):

$$\frac{\partial c(x,0)}{\partial y} + Z_2 \cdot \frac{\partial \varphi(x,0)}{\partial y} \approx 0 \tag{28}$$

Accordingly, taking the derivatives of the concentration and electrical potential functions in Eqs. (26) and (27), and inserting them into Eq. (28) gives Eq. (29):

$$B_c + Z_2 B_\varphi = 0 \tag{29}$$

Moreover, with minimal variation in concentration across the patch ($c(x,0) \approx 1$), the condition of constant electrochemical potential of counter ions at the patch [Eq. (10)] becomes Eq. (30):

$$\frac{\partial c(x,0)}{\partial x} + Z_1 \cdot \frac{\partial \varphi(x,0)}{\partial x} \approx 0 \ @\ -1 < x < 1 \tag{30}$$

Substituting Eqs. (26), (27), and (29) into Eq. (30), we obtain Eq. (31):

$$B_\varphi \cdot (Z_1 - Z_2) \cdot \left. \frac{\partial g_0(x,0)}{\partial x} \right|_{x \in [-1,1]} = 2 Z_1 \lambda \tag{31}$$

For a given value of $\lambda$, Eq. (31) requires that $\left.\frac{\partial g_0(x,0)}{\partial x}\right|_{x\in[-1,1]} \equiv a$ is a constant. Therefore,

$$B_\varphi = \frac{2Z_1\lambda}{(Z_1 - Z_2)\cdot a} \tag{32}$$

By substituting Eq. (32) into Eqs. (26) and (27) [and taking into account Eq. (29)] we obtain Eqs. (33) and (34):

$$\delta c(x,y) = -\frac{2Z_1Z_2}{(Z_1 - Z_2)\cdot aZ_1 - Z_2}\cdot\lambda\cdot g_0(x,y) \tag{33}$$

$$\delta\varphi(x,y) \equiv \varphi(x,y) + 2\lambda x = \frac{2Z_1}{(Z_1 - Z_2)\cdot aZ_1 - Z_2}\cdot\lambda\cdot g_0(x,y) \tag{34}$$

One can see that multiplication of $g_0(x,y)$ by a constant factor will not affect Eqs. (33) and (34) because any change in the function will be offset by exactly the same change in its derivative $\left.\frac{\partial g_0(x,0)}{\partial x}\right|_{x\in[-1,1]} \equiv a$. It is convenient to select $g_0(x,y)$ so that $\left.\frac{\partial g_0(x,0)}{\partial x}\right|_{x\in[-1,1]} = 1$.

For simplicity, we carry out subsequent analyses for $Z_1 = 1,\ Z_2 = -1$. In this case, Eq. (35):

$$\delta c(x,y) = \lambda\cdot g_0(x,y) \tag{35}$$

Representing this concentration perturbation at $y = 0$ in terms of the generating function [Eq. (23)] and taking into account that $g_0(x,0) = x$ since $\left.\frac{\partial g_0(x,0)}{\partial x}\right|_{x\in[-1,1]} = 1$ we obtain Eq. (36):

$$\int_{-1}^{1}\frac{F(s)}{x-s}ds = \pi\lambda x \tag{36}$$

By substituting Eq. (37) into Eq. (36) and taking the integral in the sense of the Cauchy principal value one can verify that

$$F(s) = \lambda\cdot\sqrt{1-s^2} \tag{37}$$

Thus, in the linear approximation, one can insert this $F(s)$ [Eq. (37)] into Eq. (23) to determine $\delta c(x,y)$ for any small value of $\lambda$.

### 2.4. Quadratic Approximation of Electrochemical Potential of Co-ions and Salt Concentration

Using the linear approximation for the concentration profile, we can develop a quadratic approximation for the electrochemical potential of co-ions and, hence, determine the electric field. The electrochemical potential of co-ions is especially convenient for analysis due to the extremely simple boundary condition at the wall, zero normal co-ion flux everywhere. The co-ion flux is proportional to the negative gradient of the co-ion electrochemical potential [Eq. (38)]:

$$-\vec{j}_2 = D_2\cdot c\vec{\nabla}\bar{\mu}_2 \tag{38}$$

At steady state, the flux must be conservative (no sources or sinks of ions) so [Eqs. (39) and (40)]:

$$div\left(\vec{j}_2\right) = 0 \tag{39}$$

$$\nabla^2\bar{\mu}_2 + \left(\vec{\nabla}c\cdot\vec{\nabla}\bar{\mu}_2\right) = 0 \tag{40}$$

The boundary conditions to Eq. (40) are the unperturbed linear asymptotes at negative and positive infinity (i.e. flux is constant at steady state far from the patch) and zero normal derivative of $\bar{\mu}_2$ at the wall (no co-ion flux, including the patch). The unperturbed distribution of electrochemical potential of co-ions is just a linear function of $x$ to achieve constant flux parallel to the wall. In non-dimensional variables, it is directly proportional to the dimensionless voltage drop on the patch. Therefore, it is convenient to seek a solution to Eq. (40) in the form of Eq. (41):

$$\bar{\mu}_2 \equiv 2\lambda\cdot x + \delta\bar{\mu}_2 \tag{41}$$

where $\delta\bar{\mu}_2$ is a perturbation due to the concentration-polarization phenomena.

After substitution into Eq. (40), we obtain Eq. (42):

$$\nabla^2\delta\bar{\mu}_2 + 2\lambda\cdot\frac{\partial\delta c}{\partial x} + \vec{\nabla}\delta c\cdot\vec{\nabla}\delta\bar{\mu}_2 = 0 \tag{42}$$

The supporting Information (section S4) shows how this equation can be approximately (up to the second order in $\lambda$) solved as a Poisson equation by using the Green's function method to obtain this expression for the second-order correction, $\delta\bar{\mu}_2^{(2)}$, to the distribution of electrochemical potential of co-ions ($\delta\bar{\mu}_2 \approx \lambda^2\delta\bar{\mu}_2^{(2)}$):

$$\delta\bar{\mu}_2^{(2)}(x,y) = -\frac{1}{\pi}\int_{-\infty}^{+\infty}\int_{-\infty}^{+\infty}dx'dy'\,\frac{g_0(x',y')\cdot(x-x')}{(x-x')^2+(y-y')^2} \tag{43}$$

Further, the supporting information (section S4) shows how using Eq. (43), the condition of constant electrochemical potential of counter ions at the patch surface, and the approximate expression for the salt concentration in Eq. (44):

$$c(x,y) \approx 1 + \lambda g_0(x,y) + \lambda^2 h(x,y) \tag{44}$$

one can obtain the generating function in the quadratic approximation, Eq. (45).

$$F(s) = \lambda \cdot \sqrt{1-s^2} \cdot \left(1 + \frac{\lambda}{4} \cdot s\right) \tag{45}$$

We will obtain explicit analytical expressions for the functions $g_0(x,y)$ and $h(x,y)$ below (see Eqs. (58), (59), (64)).

### 2.5. Multipole Expansion

The use of a multipole expansion to describe the function $\frac{x-s}{(x-s)^2+y^2}$ in Eq. (23) allows us to examine the symmetry and trends in the concentration profile at long distances from the patch. In turn, knowledge of the asymptotic behavior can serve as a boundary condition in numerical methods. In the multipole expansion at $\sqrt{x^2+y^2} > 1$ (sufficiently far away from the patch):

$$\frac{x-s}{(x-s)^2+y^2} \equiv \sum_{n=1} \frac{cos(n \cdot \theta)}{r^n} \cdot s^{n-1} \tag{46}$$

where we transformed to polar coordinates [Eqs. (47) and (48)]:

$$r \equiv \sqrt{x^2+y^2} \tag{47}$$

$$\theta \equiv acos\left(\frac{x}{\sqrt{x^2+y^2}}\right) \tag{48}$$

Substituting Eq. (46) into Eq. (23) yields Eq. (49):

$$\delta c(r,\theta) = \frac{1}{\pi} \cdot \sum_{n=1} \frac{cos(n \cdot \theta)}{r^n} \int_{-1}^{1} F(s) \cdot s^{n-1} ds \tag{49}$$

The strengths of all multipoles, $Q_n$,are proportional to the $(n-1)$ moments of the generating function as Eq. (50) shows.

$$Q_n \equiv \frac{1}{\pi} \cdot \int_{-1}^{1} F(s) \cdot s^{n-1} ds n = 14 \tag{50}$$

As mentioned the multipole expansion is useful because it informs us about basic features of the long-range behavior even without any numerical analysis. As one can see from Eq. (49), the dipole ($n=1$) is the longest-range multipole because of its $1/r$ dependence. Moreover, the dipole term is anti-symmetric with respect to the vertical ($y$) axis because $cos(\pi-\theta) \equiv -cos(\theta)$. Thus, if the dipole strength is not zero, at sufficiently large distances from the patch the $\delta c$ values on one side of the vertical axis are equal in absolute value and opposite in sign to the perturbations on the other side. Moreover, due to the $cos(\theta)$ dependence, the dipole perturbation is zero at $x = 0$. Qualitatively the same is true for all the odd multipoles ($n$ is odd) but their contribution additionally turns to zero at some intermediate values of angle, for example at $\theta = \frac{\pi}{6}, \frac{5\pi}{6}$ in the case of $n = 3$.

In the quadratic approximation, by using Eq. (45) all the integrals in Eq. (49) can be taken to yield Eq. (51):

$$\delta c(r,\theta) \approx \frac{\lambda}{2} \cdot \left(\frac{cos(\theta)}{r} + \frac{cos(3\theta)}{4r^3} + \right) + \frac{\lambda^2}{32} \cdot \left(\frac{cos(2\theta)}{r^2} + \frac{cos(4\theta)}{2r^4} + \right) + \tag{51}$$

Due to the symmetry of the low-voltage limit of the generating function [Eq. (37)], all the integrals with even $n$ in Eq. (49) are equal to zero in the linear approximation. Their appearance in the quadratic approximation is due to non-linear effects that give rise to a loss of symmetry of the generating function. The multipole expansion also highlights that in the linear approximation the concentration perturbation is an odd function of $x$-coordinate because only odd $n$ terms remain in Eq. (49) and these terms are odd functions of $x$ due to the $cos((2n-1)\cdot\theta)$ angular dependence.

### 2.6. Approximation of the Generating Function Calculated Numerically

Beyond the quadratic approximation, one must determine the generating function numerically. This section aims to develop a polynomial expression that describes the generating function as a function of $s$ and $\lambda$. This will allow us to describe the concentration profiles at a wide range of $\lambda$ values using a matrix of coefficients. By differentiating Eq. (23) we see that in the linear approximation the normal derivative of salt concentration at the patch close to its edges has integrable singularities of $\frac{1}{\sqrt{1-s^2}}$ kind. After integration (to obtain the generating function, $F(s)$), they give rise to abrupt drops (with diverging derivatives) of $F(s)$ at the edges. This behavior is likely due to the jump-like changes in the wall counter ion permeability that occur at the patch edges. Since this physics remains under non-linear conditions (this is confirmed by the quadratic approximation as well as numerical analysis below) we speculate that this is a general feature. To take it into account, we seek the generating function in this form:

$$F(s) \equiv \lambda \cdot \sqrt{1-s^2} \cdot K(s) \tag{52}$$

This function approaches zero at both 1 and $-1$. Eq. (52) is just a redefinition of the sought-for function, $F(s)$. However, if we additionally assume that the nonlinear-correction function, $K(s)$, is smooth and has finite derivatives everywhere including the patch edges we can represent it is a polynomial in $s$ [Eq. (53)]:

$$K(s) \equiv \sum_{m=0} A_m(\lambda) \cdot s^m \tag{53}$$

From the linear approximation, it follows that [Eqs. (54) and (55)]:

$$A_0(\lambda) \underset{\lambda\to 0}{\longrightarrow} 1 \tag{54}$$

$$A_{m>0}(\lambda) \underset{\lambda\to 0}{\longrightarrow} 0 \tag{55}$$

In the quadratic approximation $A_1(\lambda) = \lambda/4$ [see Eq. (45)]. Generally, one must determine the coefficients $A_m(\lambda)$ numerically.

By substituting Eqs. (52) and (53) into Eq. (23) we obtain Eq. (56):

$$\delta c(x,y) = \frac{\lambda}{\pi} \cdot \sum_{m=0} A_m(\lambda) \cdot \int_{-1}^{1} \frac{s^m (x-s)}{(\quad)^2 + y^2} ds \tag{56}$$

The integrals in the right-hand side of Eq. (56) have analytical expressions (see the Supporting Information section S5). Thus, in principle once the coefficients $A_m(\lambda)$ are found there is an explicit expression for the distribution of concentration perturbation [Eq. (57)].

$$\delta c(x,y) = \lambda \cdot [A_0(\lambda) \cdot g_0(x,y) + A_1(\lambda) \cdot g_1(x,y) + A_2(\lambda) \cdot g_2(x,y) + A_3(\lambda) \cdot g_3(x,y) + \quad] \tag{57}$$

where [Eqs. (58)–(61)]:

$$g_0(x,y) = x - sign(x) \cdot R_p(x,y) \tag{58}$$

$$g_1(x,y) = \left(x^2 - y^2 - \frac{1}{2}\right) + y \cdot R_m(x,y) - |x| \cdot R_p(x,y) \tag{59}$$

$$g_2(x,y) = x \cdot \left(x^2 - 3y^2 - \frac{1}{2}\right) + 2xy \cdot R_m(x,y) - sign(x) \cdot (x^2 - y^2) \cdot R_p(x,y) \tag{60}$$

$$g_3(x,y) = \left(x^2 - y^2 - \frac{1}{2}\right)^2 - 4x^2y^2 - \frac{3}{8} + y \cdot (3x^2 - y^2) \cdot R_m(x,y) + |x| \cdot (3y^2 - x^2) \cdot R_p(x,y) \tag{61}$$

and where we have denoted [Eqs. (62) and (63)]:

$$R_p(x,y) \equiv \sqrt{\sqrt{\left(\frac{x^2 - y^2 - 1}{2}\right)^2 + x^2y^2} + \frac{x^2 - y^2 - 1}{2}} \tag{62}$$

Notably, $R_p(x,y) \cdot R_m(x,y) \equiv |x|y$. Figure S1 of the Supporting Information shows plots of $g$-functions at the surface ($y = 0$) as a function of the x coordinate.

Comparison of Eqs. (44), (45), (52), and (53) shows that $h(x,y) = \frac{1}{4} g_1(x,y)$. Therefore, in the regular approximation up to quadratic terms [Eq. (64)]:

$$\delta c(x,y) = \lambda g_0(x,y) + \frac{\lambda^2}{4} g_1(x,y) \tag{64}$$

From the definitions of Eqs. (62) and (63), we see [Eqs. (65) and (66)]:

$$R_p(x,0) = \begin{cases} 0 & |x| < 1 \\ \sqrt{x^2 - 1} & |x| > 1 \end{cases} \tag{65}$$

Therefore, the concentration-perturbation distribution exactly at the wall has this relatively simple form [Eqs. (67) and (68)]:

$$\delta c(x,0) = \lambda \cdot [A_0(\lambda) \cdot x + (A_1(\lambda) + A_2(\lambda) \cdot x + A_3(\lambda) \cdot x^2) \cdot \left(x^2 - \frac{1}{2}\right) - \frac{A_3(\lambda)}{8} + \quad] \quad |x| > 1 \tag{67}$$

$$\delta c(x,0) = \lambda \cdot [[A_0(\lambda) + x \cdot (A_1(\lambda) + A_2(\lambda) \cdot x + A_3(\lambda) \cdot x^2)] \cdot \left[\left(x - sign(x) \cdot \sqrt{x^2 - 1}\right) - \frac{1}{2} \cdot (A_1(\lambda) + A_2(\lambda) \cdot x + A_3(\lambda) \cdot x^2) - \frac{A_3(\lambda)}{8} + \quad\right] \quad |x| > 1 \tag{68}$$

which, in the regular second-order approximation, reduces to Eqs. (69) and (70):

$$\delta c(x,0) = \lambda \left(x + \frac{\lambda}{4}\left(x^2 - \frac{1}{2}\right)\right) \quad |x| > 1 \tag{69}$$

$$\delta c(x,0) = \lambda \cdot \left[\left(1 + \frac{\lambda x}{4}\right) \cdot \left(x - sign(x) \cdot \sqrt{x^2 - 1}\right) - \frac{\lambda}{8}\right] \quad |x| > 1 \tag{70}$$

The leading term of the long-range asymptotics is Eq. (71):

$$\delta c(x,0) \underset{|x|\to\infty}{\longrightarrow} \left(A_0(\lambda) + \frac{A_2(\lambda)}{4} + \right) \cdot \frac{1}{2|x|} \tag{71}$$

Or Eq. (72):

$$\delta c(x,0) \underset{|x|\to\infty}{\longrightarrow} \frac{1}{2|x|} \tag{72}$$

in the regular second-order approximation ($A_0(\lambda) = 1$ and other coefficients in Eq. (71) are zero in this approximation).

The terms with odd-indexed $A$-coefficients (arising due to non-linear phenomena) decay more rapidly, namely $\sim 1/x^2$.

At $y \neq 0$, a simple expression can be obtained far away from the patch (long range). In this case, one can use the multipole expansion of Eq. (49) to obtain Eq. (73):

$$\delta c(r,\theta) \equiv \frac{\lambda}{\pi}\cdot\sum_{n=1}\frac{\cos(n\bullet\theta)}{r^n}\sum_{m=0}A_m(\lambda)\cdot\int_{-1}^{1}\sqrt{1-s^2}\cdot s^{m+n-1}ds \approx \frac{\lambda}{2}\cdot\left[\frac{\cos(\theta)}{r}\cdot\left(A_0(\lambda)+\frac{A_2(\lambda)}{4}+\right)+\frac{\cos(2\theta)}{r^2}\cdot\left(\frac{A_1(\lambda)}{4}+\frac{A_3(\lambda)}{8}+\right)+\frac{\cos(3\theta)}{r^3}\cdot\left(\frac{A_0(\lambda)}{4}+\frac{A_2(\lambda)}{8}+\right)+\frac{\cos(4\theta)}{r^4}\cdot\left(\frac{A_1(\lambda)}{8}+\frac{5}{64}A_3(\lambda)+\right)+\right] \quad (73)$$

Comparison of Eq. (73) with the multipole expansion obtained in the quadratic approximation [Eq. (51)] shows that non-linear effects (beyond the quadratic approximation) not only cause appearance of non-zero quadrupole ($n=2$) and octupole ($n=4$) terms but also give rise to modification of dipole ($n=1$) and sextupole ($n=3$) strengths. Even multipole distributions are symmetric functions of the $x$-coordinate. Therefore, the appearance of even multipoles indicates deviations (under non-linear conditions) from the antisymmetric pattern in the salt-perturbation distribution occurring at weak fields. One can also see that the long-range asymptotics (dominated by the dipole) ~~result~~ from the same combination of coefficients as the asymptotics at the wall [Eq. (71)].

### 2.7. Summary of Theory Section

This section briefly summarizes and emphasizes the most important points in the theory. The first section defined the governing dimensionless equations, Eqs. (5) and (6), and boundary conditions for the problems. Subsequently, we derived Eq. (23), which describes the concentration distribution in terms of the generating function, $F(s)$, which one can determine from numerical data using Eq. (24). Fitting of a set of $F(s)$ functions (obtained at different $\lambda$ values) using Eqs. (52) and (53) allows expression of the concentration profiles from Eqs. (57)–(63). Below we will show how using polynomial approximations for the $A$-coefficients in Eq. (53) one can obtain full concentration profiles over a wide range of $\lambda$ values using a small matrix of coefficients.

The theory section also provides linear and quadratic approximations that give concentration profiles at low to moderate $\lambda$ values. Eqs. (35) and (58) describe the concentration profile in the linear approximation, and Eqs. (44), (58), and (59) with $h(x,y)=\frac{1}{4}g_1(x,y)$ describe the quadratic-approximation concentration profile. Finally, Eqs. (43) and (58) allow calculation of the electrochemical potential of the co-ions, which in turn will enable determination of the local electric field.

The subsection on multipole moments showed that at low values of $\lambda$ the concentration profile is antisymmetric about $x=0$. Moreover, regardless of $\lambda$, the concentration will decay with $1/r$ at long distances from the patch. As $\lambda$ increases even multipole moments will lead to non-antisymmetric distributions.

### 2.8. Numerical Procedures

Beyond the linear and quadratic assumptions, calculations of concentration and potential distributions require numerical methods. However, numerical methods often suffer from substantial computational errors. For example, some of the boundary conditions to this problem [Eqs. (13) and (14)] are set at negative and positive infinity, but numerically the problem can be solved only within a finite domain. As we have seen above [see Eq. (49)], the concentration perturbation decays quite slowly (inversely proportional) with the distance from the patch. Therefore, setting the concentration perturbation equal to zero at a moderate distance from the patch can give rise to substantial error, particularly at long range. At the same time, using very large computational domains (in combination with sufficiently fine meshing close to the patch) is difficult in view of increases in the computation time. To solve this problem, we used the fact that at large distances from the patch the distribution of concentration perturbation depends on the distance and angle (in polar coordinates) as the field of a dipole. Under non-linear conditions, its strength is unknown and had to be found iteratively. As the criterion of convergence of iterations, we used the condition of matching $r$-derivatives calculated numerically just inside the semi-cylindrical external boundary of the computational domain and analytically (using the large-distance asymptotics) just outside it. Strictly speaking, the long-range asymptotics also have some contributions from higher multipole moments, which we neglected. However, due to their more rapid decay with distance this caused only minor errors.

We solved the problem numerically using COMSOL Multiphysics software, version 5.0.1.276, with the Nernst Planck Equations module (chnp). The computational domain had a semi-cylindrical shape with a radius of 20, while the patch half-width was set equal to one (in dimensionless coordinates). We used a basic triangular mesh with a maximum element size of 0.05, a minimum element size of $10^{-4}$, a maximum element growth rate of 1.1, a resolution of curvature of 0.2, and a resolution of narrow region of 1. The mesh was additionally refined close to the patch edges ($<0.2$ from the edges) as much as 8 times along the $y$-axis and 16 times along the $x$-axis.

## 3. Results and Discussion

This section first presents some numerical concentration profiles and examines their accuracy compared to the quadratic approximation that applies at low to moderate values of $\lambda$. Subsequently, we compute the generating function and approximate it using the polynomial $K(s)$ [Eq. (53)]. This allows representation of the two-dimensional concentration profiles over a wide range of $\lambda$ values using a $4\times7$ matrix of coefficients, half of which are zero. Without such a function, one can only present large two-dimensional arrays for concentration profiles at a few values of $\lambda$. Subsequently, we describe the specific ion fluxes as well as electric-field distributions at low fields. These distributions give an initial idea of trends that could prove

useful in patch-based preconcentration. Finally, we suggest future work in this area.

### 3.1. Numerical Salt Concentration Profiles

Numerical calculations show extensive concentration polarization above the patch. Figure 7A plots dimensionless concentration as a function of the distance $y$ from the patch for a $\lambda$ value of 1.558. (Figure S2 gives a color-intensity plot of the two-dimensional concentration profile.) At the patch surface ($y = 0$) the concentration at the right edge of the patch ($x = 1$) is almost 80 times greater than at the left edge ($x = -1$) in Figure 7A. Remembering that $\lambda \equiv \frac{FE_0 l}{2RT}$, for a patch width of 2 mm (half width $l$ of 1 mm), $\lambda = 1.558$ corresponds to 80 V/m. With a patch width of 20 μm, $\lambda = 1.558$ would give an electric field of 8 kV/m.

As Figure 7A shows, the concentration polarization gradually decreases on moving away from the patch in the vertical direction. However, the ratio of concentrations at the two edges of the patch is still nearly 3 at 500 μm above a patch with a half-width of 1 mm ($y = 0.5$).

Figure 7B shows the concentration profiles at the surface of a patch ($y = 0$) for different values of $\lambda$. As expected, the extent of concentration polarization decreases as the strength of the electric field or the patch width decreases. The data indicate that larger patches will give rise to greater concentration polarization (the value of $\lambda$ increases linearly with the patch width), which could allow the use of smaller electric fields. Moreover, larger patches will lead to concentration polarization at greater distances from the patch.

Due to their finite mesh size, numerical methods are always approximations. To examine the extent of numerical errors, we compared values of concentration perturbation obtained numerically and with the quadratic solution, which is highly accurate at values of $\lambda < 0.5$. As Figure 8 shows, the two methods give similar trends, although there are small but significant differences between their $\delta c$ values. This is particularly evident at the two edges of the patch ($x = -1$ *and* $x = 1$) where concentrations change rapidly. One would expect numerical solutions to show the most error in such regions. However, there are also rather surprising significant deviations (about 10%, Figure 8B) at larger distances from the patch. Below we provide a semi-empirical method for overcoming some of these numerical errors. Nevertheless, the discrepancies in the numerical method and the quadratic solution values of $\delta c$ are less than 20% (Figure 8B), so the numerical results should show the important trends that occur in these systems.

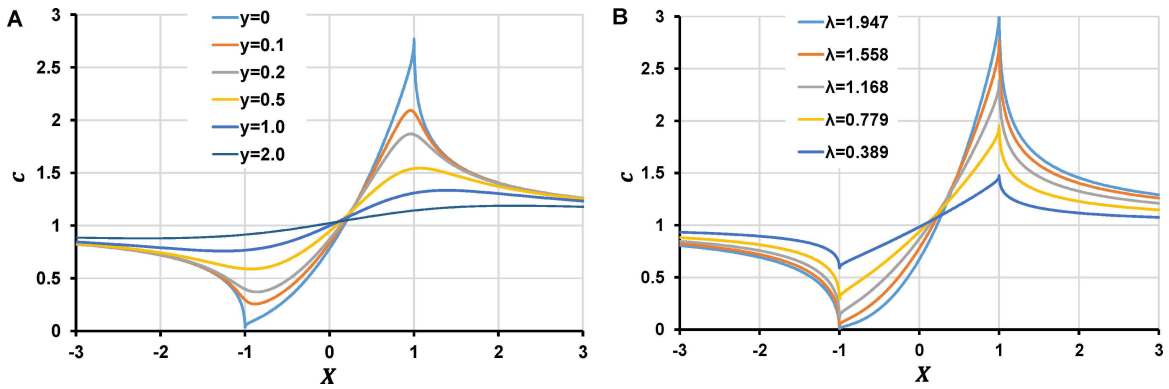


**Figure 7.** Plots of dimensionless concentration, $c$, profiles at A) different distances from the wall with $\lambda = 1.558$, and B) at the wall with different values of $\lambda$. The x-coordinate is scaled on the patch half width (Figure 6 shows the coordinate system.)

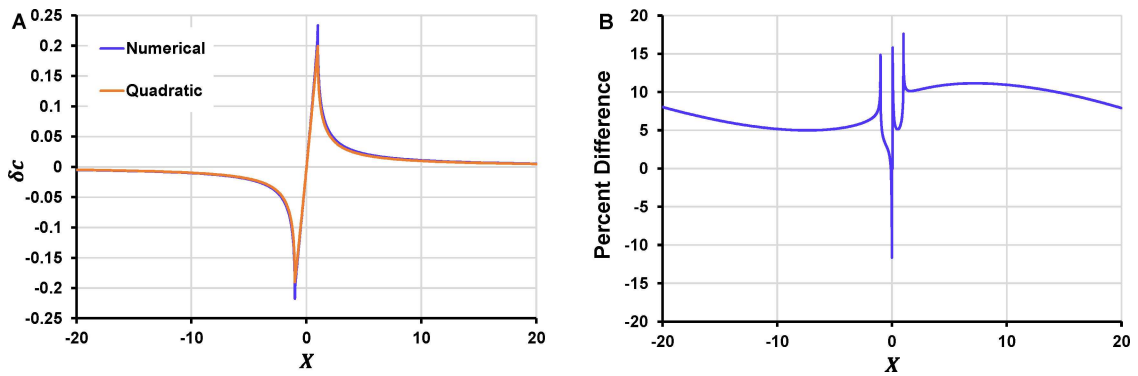


**Figure 8.** A) Plots of concentration perturbation ($\delta c = c - 1$) obtained using a full numerical solution and the quadratic approximations [Eqs. (69) and (70)] at $y = 0$ for $\lambda = 0.1947$. B) The percent difference between $\delta c$ values for the quadratic solution and the numerical method. The large differences near $x = 0$ result from the change in sign in the value of $\delta c$ in this region and do not stem from large differences in the methods.

### 3.2. Representation of Concentration Profiles in Terms of the Generating Function, and Correcting Numerical Data

The above numerical data show important trends in concentration profiles, but it is not possible to present two-dimensional distributions of concentration perturbation at various $\lambda$ values in an exhaustive, quantitative way. To overcome this challenge, we employ the generating function, $F(s)$, which at a given $\lambda$ provides full two-dimensional concentration distributions using Eq. (23). Parameterization of this function (see the next section) using a matrix of coefficients subsequently allows calculation of the concentration profiles over a wide range of $\lambda$ values using Eqs. (57)–(63). Importantly, the generating function also allows correction of numerical data.

Figure 9 shows the generating function, $F(s)$, determined at different values of $\lambda$. We obtained $F(s)$ using numerical data and Eq. (24). As this equation shows, calculation of $F(s)$ requires taking the $y$-derivatives of the numerical concentration data at the patch surface and then integrating these derivatives from the left side of the patch to a given coordinate. The abrupt drops in the generating function at the patch edges persist at all voltages. In Eq. (52), we define $F(s) \equiv \lambda \cdot \sqrt{1-s^2} \cdot K(s)$. The $\sqrt{1-s^2}$ part of the function allows it to model the abrupt drops at the edge of the patch where $s = 1$ *or* $-1$.

With increasing voltage, $F(s)$ progressively loses symmetry with respect to the vertical axis and is ever more skewed to the right. In the multipole approximation in Eq. (49) the asymmetry corresponds to the rise of nonzero even ($n = 2, 4, \ldots$) multipole moments. Additionally, the integral of the function that controls the strength of the dipole ($n = 1$) moment in Eq. (50) increases with voltage more slowly at larger voltages so $F(s)$ increases more slowly at higher $\lambda$ values (note that in Figure 9 the dimensionless voltage drops, $\lambda$, increase with a constant increment).

Figure 10 show the strengths of the first four multipole moments, $Q_n$, determined using Eq. (50). The strength of the odd moments ($n = 1, 3$) initially increases linearly with the applied voltage, which reflects their occurrence already in the linear approximation. The even moments ($n = 2, 4$) appear only in the quadratic approximation since they are due to non-linear concentration-polarization phenomena [see Eq. (51)].

Using Eq. (52), we also determined the function $K(s)$ at different values of $\lambda$. Figure 11 shows some examples of numerically calculated $K(s)$ functions. The dramatic drops in $K(s)$ at the patch edges likely stem from numerical errors. Consistent with this supposition, Figure 12 shows that the non-linear correction function calculated numerically for a very low applied voltage is not unity, even when the linear approximation is perfectly applicable and $K(s)$ should be equal to one everywhere [compare Eq. (52) and Eq. (37)]. Due to numerical errors, there are deviations of a few percent from unity in the middle of Figure 12 and dramatic deviations at the edges. As the figure shows, the use of a finer mesh reduced the difference from unity (at least in the center), confirming that these deviations stem from numerical error. The Supporting Information shows that these deviations probably arise because Comsol Multiphysics outputs normal derivatives not exactly at the boundary of the numerical domain but at some short distance from it (section S8).

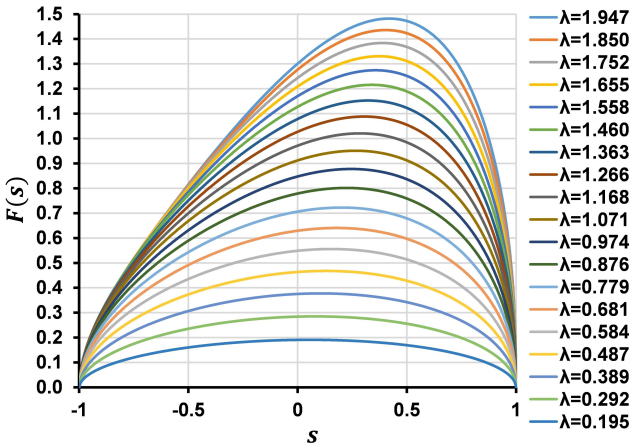


**Figure 9.** Plot of the generating function $F(s)$ calculated for a number of dimensionless voltage drops on the patch (the legend shows the corresponding values of parameter $\lambda$). $F(s)$ was calculated using numerical data and Eq. (24).

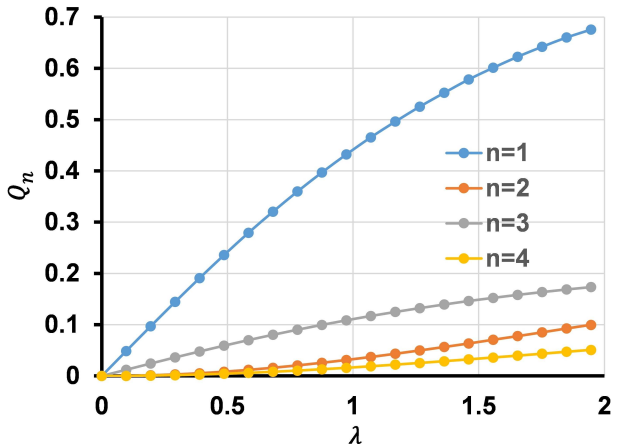


**Figure 10.** Strengths of the first four multipole moments vs dimensionless voltage drop, $\lambda$.

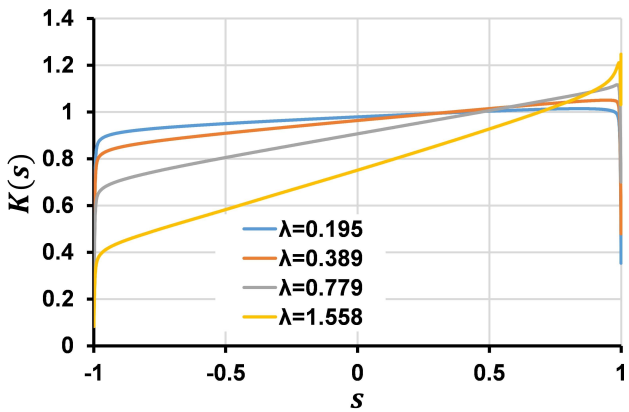


**Figure 11.** Plot of the non-linear-correction function, $K(s)$, calculated from numerical data for several dimensionless voltage drops ($\lambda$).

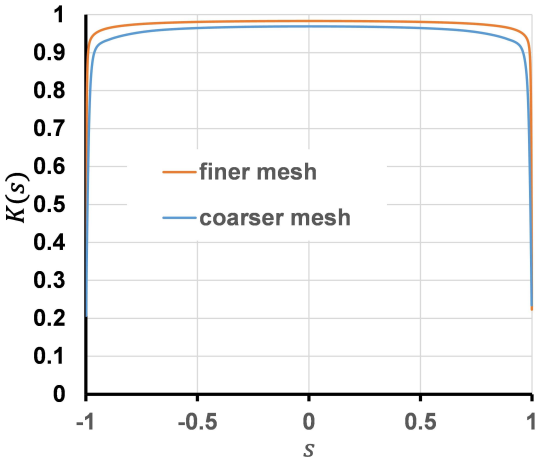


**Figure 12.** Non-linear-correction function, $K(s)$, calculated numerically for $\lambda = 1.947 \cdot 10^{-4}$. Theoretically the value should be unity everywhere.

These effects cause the numerical solution for the generation function to deviate from the regular linear approximation by ~2 percent even at very low dimensionless voltage drops. To account for this (as well as reduce the effect of the dramatic drops at the edges) we corrected all the generation functions via multiplying them by the reciprocal of the function from Figure 12 calculated with the finer mesh (the same mesh was used for all the calculations of generating function). Concentrations obtained with the corrected generation function and Eq. (23) agreed perfectly with the regular perturbations [Eq. (45)] at low to moderate dimensionless voltage drops. However, the correction might introduce some error at larger $\lambda$, where we have no data for comparison.

### 3.3. Approximating the Generating Function using Polynomials

The next step is approximating (at each voltage drop) the non-linear-correction function, $K(s)$, with polynomials of coordinate according to Eq. (53). By substituting Eqs .(52) and (53) into Eq. (73), specifying this equation for the first four multipole moments, taking the integrals analytically as in Eq. (73) and solving the resulting system of linear equations for the $A_m(\lambda)$ coefficients, we obtain Eqs. (74)–(77):

$$A_0(\lambda) = \frac{4}{\lambda} \cdot (Q_1(\lambda) - 2Q_3(\lambda)) \tag{74}$$

$$A_1(\lambda) = \frac{8}{\lambda} \cdot (5Q_2(\lambda) - 8Q_4(\lambda)) \tag{75}$$

$$A_2(\lambda) = \frac{16}{\lambda} \cdot \left(2Q_3(\lambda) - \frac{Q_1(\lambda)}{2}\right) \tag{76}$$

$$A_3(\lambda) = \frac{64}{\lambda} \cdot (2Q_4(\lambda) - Q_2(\lambda)) \tag{77}$$

Figure 13 shows the first four coefficients of the polynomial representation of the non-linear-correction function calculated from the strengths of multipole moments (shown in Figure 10) for a range of dimensionless voltage drops. The lines in the figure show polynomial approximations of those coefficients as functions of $\lambda$ (see below). In agreement with the increased skewing at higher $\lambda$ (see Figure 9), the $A_1(\lambda)$ coefficient that controls the linear term of the polynomial increases rapidly as $\lambda$ increases. The coefficient of the space-independent term, $A_0(\lambda)$, (the figure shows its deviation from the limiting value of one, which corresponds to the linear approximation) controls the progressive downward shift of the nonlinear-correction function with increasing voltage (see Figure 11). The role of the other two terms is subtler but their magnitude is noticeably smaller (at least, within the investigated voltage range).

The use of the coefficients in Figure 13 gives rise to approximations of the generating function that are visually indistinguishable from the numerically calculated functions. To quantify the accuracy of the approximations, we compared the multipoles calculated using the coefficients and Eq. (73) with the multipoles calculated using the numerical generating function and Eq. (50). The polynomial approximation-related relative errors for $n = 1, 2,$ *and* 3 were vanishingly small (below 0.02%). Only the $n = 4$ moment featured a relative error of $1.8 \pm 0.07$% that was practically independent of voltage.

The final step in expressing a wide range of concentration distributions in terms of a relatively simple matrix of coefficients is to fit the values of $A_n(\lambda)$ to polynomials. A change in the direction of the applied electric field should give rise to a mirror reflection of the nonlinear-correction function with respect to the vertical axis. In view of this, the coefficients $A_0(\lambda)$ and $A_2(\lambda)$ should be even functions of $\lambda$ and the coefficients $A_1(\lambda)$ and $A_3(\lambda)$ should be odd functions of $\lambda$. We kept this in mind when defining polynomial approximations for the dependences in Figure 13, using only even powers for $A_0(\lambda)$ and $A_2(\lambda)$ and only odd powers for $A_1(\lambda)$ and $A_3(\lambda)$. Table 1 shows the coefficients of the polynomial approximations of $A_n(\lambda)$. With these coefficients, one can calculate the two-dimensional distributions of concentration perturbation for any value of dimensionless voltage drop on the patch from the investigated range ($|\lambda| < 2$).

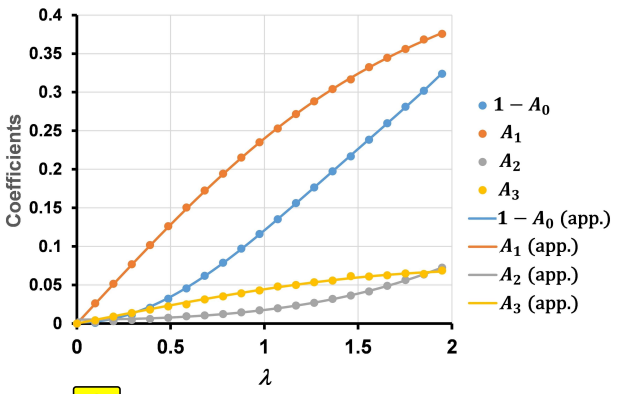


**Figure 13.** $1 - A_0$) coefficients as a function of $\lambda$ as well as their polynomial approximations (app.).

**Table 1.** Coefficients of polynomial approximations of $A_n(\lambda)$.

| | $\lambda^0$ | $\lambda^1$ | $\lambda^2$ | $\lambda^3$ | $\lambda^4$ | $\lambda^5$ | $\lambda^6$ |
|---|---|---|---|---|---|---|---|
| $A_0$ | 0.998917 | 0 | −0.1402 | 0 | 0.022597 | 0 | −0.00214 |
| $A_1$ | 0 | 0.26267 | 0 | −0.02429 | 0 | 0.001595 | 0 |
| $A_2$ | 0.005145 | 0 | 0.010301 | 0 | 0.002242 | 0 | −7.1E-05 |
| $A_3$ | 0 | 0.048429 | 0 | −0.00405 | 0 | 0.00011 | 0 |

Figure 13 and Table 1 show that at low voltages $A_0(\lambda)$ tends almost exactly to one as it should according to the result available in the linear approximation [compare Eqs. (37), (52), (53)]. However, the deviation of $A_1(\lambda)$ from the value of 0.25 predicted in the quadratic approximation [compare Eqs. (45), (52), and (53)] is around 5%. Probably, this is due to our use of only a finite number of terms in the polynomial approximation of the non-linear correction function [Eq. (53)]. As a result, the retained terms somehow "take over" the contribution of neglected terms.

In the Supporting Information (see FigureS4), we compare calculation of the concentration-perturbation distribution using the polynomial approximations for $A_n(\lambda)$ with the rigorous quadratic approximation at $\lambda = 0.1947$ where this approximation should have a high accuracy. The percent difference between the polynomial and quadratic approximations are less than 0.5% (with the exception of a couple of points inside the patch where the function changes sign). Thus, the correction procedure introduced above to reduce the numerical error in the generating function is quite effective (at least, at lower $\lambda$ values). Moreover, the distribution obtained using the polynomial approximations and the corrected generation function is better than the original numerical data (compare Figure 8 and Figure S4). Correction of the generation function overcomes some of the numerical error.

### 3.4. Trends in Concentration Distributions and a Simplified Approximation

Figure 14 shows the concentration distributions calculated (using the coefficients in Table 1) at the wall for several dimensionless voltage drops on the patch. Note that unlike Figure 7, these plots do not show spikes (upward or downward) at the patch entrance and exit. At higher $\lambda$ values, the progressive extension of the depleted zone towards the "exit" results from a kind of local limiting-current phenomenon. The current can "enter" the patch, but the depletion phenomenon itself limits the current density. Consequently, with increasing voltage additional current must "enter" ever more to the right where strong diffusion from the immediately adjacent enrichment zone limits the salt depletion. As the depletion zone extends there is a decreasing area for the current to "exit" the patch. This gives rise to an ever larger "exit" current density as well as a narrower and higher enrichment increase. The Supporting Information (Figure S5) quantifies the extent of these phenomena via comparison of $x$-derivatives of salt

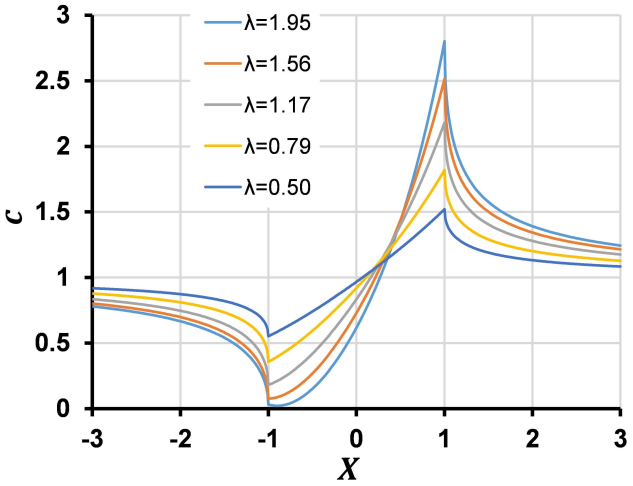


**Figure 14.** Dimensionless concentration at the wall ($y = 0$) at various dimensionless voltage drops, as calculated using the polynomial coefficients in Table 1 and Eqs. (57)–(63).

concentration at the patch surface at $x = -1$ (patch "entrance") and $x = 1$ (patch "exit").

The quadratic approximation [Eq.(64)] reflects the "skewing" of the generation function to the right with increasing dimensionless voltage drop, but it does not take into account the progressive overall shift of the non-linear correction function, $K(s)$, downwards as seen in Figure 11. This trend results in a decrease of the $A_0$ coefficient with increasing $\lambda$. In the table of coefficients of the polynomial approximations, this trend appears in the third order in $\lambda$. We do not have regular-perturbation analytical results that are accurate where the third-order $\lambda$ term is significant. Nonetheless, we modified the quadratic approximation using the numerical values of the $A_0$ coefficient instead of value of one. Remarkably, this correction is largely sufficient to reproduce the dimensionless-concentration-perturbation profiles with accuracy better that 2–3% at $\lambda \leq 1.5$. Moreover, outside the patch ($|x| > 1$, especially at positive $x$) such an approximation works quite well even at $\lambda \approx 2$. However, within the patch especially close to the "entrance" point there are noticeable deviations. At the same time, within the "enriched" part of the solution over the patch the agreement is still excellent. Figure 15 illustrates these points.

In this simplified approximation one can just use the polynomial approximation for $A_0(\lambda)$ with the numerical coefficients given in Table 1. However, Eq. (78) very accurately approximates the dependence of $A_0$ on $\lambda$.

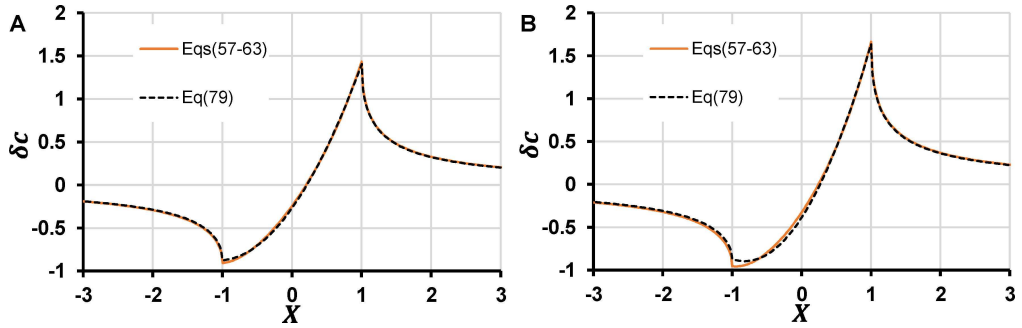


**Figure 15.** Dimensionless concentration perturbation calculated via the full approximation of Eqs. (57)–(63) and via its simplified version in Eq. (79). The profiles are those at ($y = 0$) for A) $\lambda = 1.460$ and B) $\lambda = 1.753$.

$$A_0(\lambda) \approx 1 - \frac{\lambda^2}{8} \cdot \left(1 - \frac{\lambda^2}{12}\right) \tag{78}$$

By substituting Eq. (78) instead of one into the quadratic approximation [Eq. (64)] we obtain this relatively simple expression Eq. (79):

$$\begin{aligned} &\delta c(x,y) \approx \lambda \cdot \left(1 - \frac{\lambda^2}{8} \cdot \left(1 - \frac{\lambda^2}{12}\right)\right) \cdot \\ &\left(x - sign(x) \cdot R_p(x,y)\right) \\ &+ \frac{\lambda^2}{4} \cdot \left[\left(x^2 - y^2 - \frac{1}{2}\right) + |x| \cdot \left(\frac{y^2}{R_p(x,y)} - R_p(x,y)\right)\right] \end{aligned} \tag{79}$$

where we have additionally taken into account that $R_p(x,y) \cdot R_m(x,y) \equiv |x|y$ as can be seen from the definitions of these functions [Eqs. (62) and (63)].

### 3.5. Co-Ion Flux Distribution

Thus far, we focused on the distribution of concentration perturbations because they are of primary practical interest. Moreover, one can present a large amount of data in a relatively simple way in terms of the generating function and its moments. Nonetheless, the ion electrochemical potentials are also important as they allow calculation of ion fluxes as well as the electric field. The next three sections provide methods for approximating the distribution of ion fluxes and the electric field and give a physical picture of these quantities.

In the Theory section we derived an explicit expression in quadratures for the second-order correction to the distribution of the electrochemical potential of co-ions[Eq. (43)]. This enables us to obtain Eqs. (80) and (81), which express co-ion flux components that are valid up to the second order approximations in $\lambda$. This approximation is reasonably valid for $\lambda \leq 0.7$.

$$-j_{2x} \sim c \cdot \frac{\partial \bar{\mu}_2}{\partial x} \approx 2\lambda + \lambda^2 \cdot \left(2g_0 + \frac{\partial \delta \bar{\mu}_2^{(2)}}{\partial x}\right) \tag{80}$$

$$-j_{2y} \sim c \cdot \frac{\partial \bar{\mu}_2}{\partial y} \approx \lambda^2 \cdot \frac{\partial \delta \bar{\mu}_2^{(2)}}{\partial y} \tag{81}$$

The first term on the right-hand side of Eq. (80) corresponds to the unperturbed tangential flux of co-ions directed from right to left. The second term, $\lambda^2 \cdot \left(2g_0 + \frac{\partial \delta \bar{\mu}_2^{(2)}}{\partial x}\right)$, is the perturbation due to the concentration polarization. The unperturbed vertical flux, $j_y$, is zero so the quadratic correction in Eq. (81), $\lambda^2 \cdot \frac{\partial \delta \bar{\mu}_2^{(2)}}{\partial y}$, is proportional to the total vertical flux as well as to its perturbation. $\frac{\partial \delta \bar{\mu}_2^{(2)}}{\partial y}$ values were obtained via numerical double integration as shown in Eq. (43), and the $g_0$ function is given by Eq. (58).

Figure 16 shows the vector field proportional to the co-ion flux perturbations in Eqs. (80) and (81) (actually, perturbation of product of concentration and negative gradient of electrochemical potential of co-ions) divided by $\lambda^2$. Because the net co-ion flow is from right to left (negative), a positive $x$-component correction means that the horizontal flux is smaller (in absolute value) than the unperturbed flux. Similarly, a

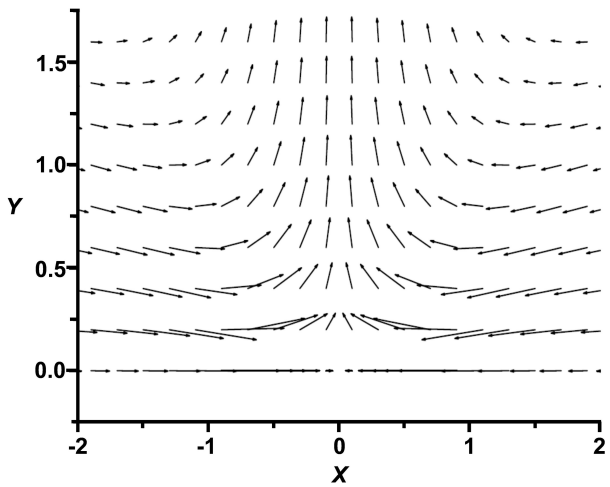


**Figure 16.** Perturbation of co-ion fluxes divided by $\lambda^2$. The perturbation is the difference between the local flux and the flux far away from the patch. The correction employs the quadratic approximation [Eq. (43)], which is reasonable for $\lambda < 0.7$.

negative *x*-component correction indicates increased flux relative to the unperturbed value. With our choice of signs, at positive *x* the concentration increases (relative to the unperturbed value). Close to the wall this increase in the concentration is only partially compensated by a decrease in $\frac{\partial \bar{\mu}_2}{\partial x}$ so overall the tangential-flux magnitude, $c \cdot \frac{\partial \bar{\mu}_2}{\partial x}$, increases here. At negative *x*, the situation is opposite, the concentration decreases and the increase in the electrochemical potential gradient does not completely compensate this concentration decrease.

One can also think of transport in terms of diffusive and electromigration components. Based on the concentration profiles in Figure 7, at low fields the concentration gradient above the patch is approximately constant. This should result in diffusion that enhances the co-ion flux from right to left above the patch. However, electromigration slows sufficiently to the left of zero (due to lower concentration) such that the magnitude of the flux decreases above the patch in this region. Note that electromigration decreases with concentration, but it also depends on the electric field.

As Figure 16 shows, the magnitude of the tangential-flux-component correction varies along the *x*-coordinate. To maintain steady state ion concentrations, this variation requires the appearance of corresponding vertical fluxes. Remarkably, the vector field shown in Figure 16 is universal since it does not depend on any problem parameters, as long as the value of $\lambda$ is not too large.

### 3.6. Counter Ion Fluxes

The ion-exchange patch perturbs the concentration and electric field profiles because it allows a low-resistance pathway for current flow via counter ions. However, the net flow of counter ions into the patch must be zero to avoid ion accumulation. Thus, we expect counter ions to enter the patch near one end and exit at the other. In contrast to the co-ions, for counter ions there is a non-zero perturbation to their flux already in the linear approximation. To calculate the counter ion flux in this approximation, we used this relationship [Eq. (82)]:

$$\vec{j}_1 \sim -c \cdot \vec{\nabla}\bar{\mu}_1 \equiv -c \cdot 2\vec{\nabla} ln(c) - \vec{\nabla}\bar{\mu}_2 \approx 2\lambda \cdot (\vec{i}_x - \vec{\nabla} g_0) \quad (82)$$

where $\vec{i}_x$ is the unit vector in the *x*-direction resulting from the constant unperturbed counter ion flux along the x-axis.

Figure 17 shows the vector field $(\vec{i}_x - \vec{\nabla} g_0)$ in Eq. (82). As expected the counter ions enter the patch on the left side and exit at the right. The perturbation of the flow pattern becomes smaller as one moves away from the patch. At larger fields the picture will become asymmetric, but the principal feature will remain of counter ions entering and leaving the patch at its different parts.

As with co-ions, we can consider counter ion fluxes in terms of diffusive and electromigration components. The net counter ion flux is from left to right. However, counter ion diffusion will occur from right to left based on concentration profiles in Figure 7. At the surface of the patch, electrical migration exactly compensates diffusion to give zero flux in the *x*-direction.

### 3.7. Electric Fields

To obtain an expression for the gradient of electrostatic potential (electric field is proportional to the negative gradient of potential) we use the definition of electrochemical potential of co-ions to obtain in the linear approximation [Eq. (83)]:

$$\vec{\nabla}\varphi \equiv \vec{\nabla} ln(c) - \vec{\nabla}\bar{\mu}_2 \approx \lambda \cdot (\vec{\nabla} g_0 - 2 \cdot \vec{i}_x) \quad (83)$$

Figure 18 shows the distribution of $\vec{\nabla}\varphi$ scaled on $\lambda$. We present the negative dimensionless electric field, so the vectors are proportional to the electrical force that a trace negatively-

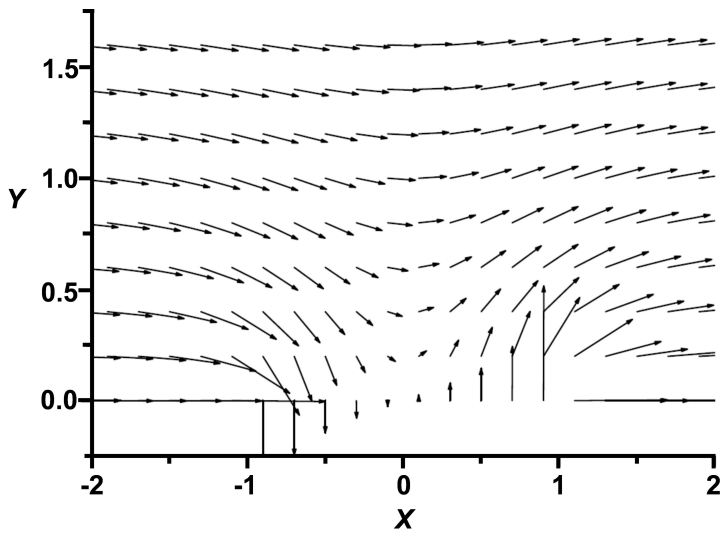


**Figure 17.** Vector field proportional to counter ion fluxes divided by $2\lambda$ as calculated at weak electric fields in the linear approximation. (Note that these are proportional to fluxes and not flux perturbations.)

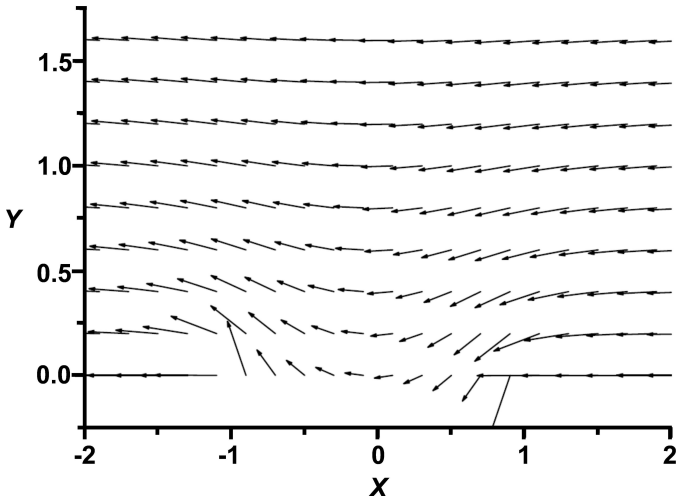


**Figure 18.** Distribution of negative dimensionless electric field (linear approximation, $\vec{\nabla} g_0 - 2 \bullet \vec{i}_x$) scaled on $\lambda$. (Fluxes of co-ionic traces immediately after their introduction in a constant concentration are proportional to this vector.)

charged co-ion might experience in preconcentration. They are also proportional to the flux of the trace co-ion at uniform concentration. The electrical force on such co-ions is from right to left in the bulk solution. Just above the patch (close to $x = 1$) however, the right to left electrical force decreases, and the co-ions experiences a downward force at the right side of the patch and an upward force at the left. Nevertheless, these ions will not enter a perfectly selective ion-exchange patch.

Interestingly the electric field in the *x*-direction is not zero at the patch surface despite the assumption of "infinite conductivity" (constant counter ion electrochemical potential) in the patch. Both the electric field and the concentration gradient drive counter ion transport at the patch. Thus, the concentration gradient at the patch surface (see Figure 14 for example) would lead to infinite current (with an infinitely conductive patch) in the absence of an electric field. The electric field leads to counter ion electromigration that exactly compensates diffusion (see Figure 17) in the *x*-direction at the patch surface.

## 4. Conclusions

We carried out a detailed parametric study of the current-induced concentration polarization near a perfectly permselective band-like ion-exchange patch inserted in an infinite insulating wall. An exhaustive concentration-polarization analysis is possible because (due to the system simplicity) the concentration distribution depends on only a single dimensionless parameter proportional to the dimensionless drop of applied voltage on the patch width. We obtained rigorous analytical results up to second-order perturbations in the dimensionless parameter (low to moderate dimensionless voltage drops). At higher voltages, the problem was solved numerically. Additionally, semi-numerical approximations provide reasonable accuracy within a broad range of applied voltages while the regular-perturbation analytical result is more accurate at relatively weak fields but fails at larger values of $\lambda$.

The principal physical feature of the solution is the appearance of neighboring depletion and enrichment zones. At weak applied fields, the extents of depletion and enrichment as well as the dimensions of these two perturbation zones are the same. With increasing applied voltage, the depletion zone becomes ever broader at the expense of the enrichment zone, which gets narrower while its magnitude increases super-linearly. The conditions of closely co-located depletion and enrichment zones may be beneficial for counter-gradient trace-analyte focusing. In such a system increased convective co-flow within the enrichment zone accompanies enhancement of electromigration counter-flow within the depletion zone, which may enhance sample focusing.

Presentation of the two-dimensional concentration distributions in the form of Eq. (23) is useful because the whole parametric study reduces to a family of $F(s)$ curves calculated for a range of values of dimensionless voltage drop (Figure 9). Importantly, one can approximate these functions using a combination of simple functions [Eqs. (52) and (53)]. We found the coefficients of these functions numerically and approximated them with relatively simple polynomials of $\lambda$. Finally, a $4 \times 7$ table of coefficients of polynomial approximations of four $A_n(\lambda)$ coefficients describes the results of the complete parametric study. Any interested reader can use them with Eqs. (57)–(63) to reproduce our results (an unusual situation with numerical studies). Note that this is not a formal fitting of functions of two variables (which would be very difficult in view of finding a suitable functional form that reflects all the features of concentration distributions shown in Figure 7); the functional form has a clear origin.

## 5. Future Directions

In this study, we limited ourselves to the first four terms in the polynomial approximation of function $K(s)$. Those are largely sufficient within the voltage range we investigated (going beyond this range would be difficult in view of numerical problems anyway). However, in principle, in future work one could extend this approach towards higher-order terms. All the corresponding integrals can be taken analytically. Therefore, our analysis can be straightforwardly extended towards still higher voltages just following the outlined algorithm. Perhaps more importantly, one could easily extend the analysis to include an opposite wall (with a similar patch or without).

Including non-zero volume flow will require more essential modifications because the Laplace equation will no longer describe the concentration profile. Additionally, accounting for flow will require a numerical solution that includes the Navier–Stokes and continuity equations. Overall, flow will likely lead to decreased concentration polarization for the dominant salt in solution if the sign of the fixed charge in the patch and the wall is the same. If the signs of these charges are opposite, the system is more complex and probably more interesting. The

results of this study will be useful, at least as a reference case, to validate the numerical procedures.

## List of Symbols

| | |
|---|---|
| $a$ | constant representing $\left.\frac{\partial g_0(x,0)}{\partial x}\right\|_{x\in[-1,1]}$ |
| $A_m(\lambda)$ | coefficients of the nonlinear-correction function, see Eq. (53) |
| $B_c, B_\varphi$ | constants for solving concentration profiles in the linear approximation |
| $c$ | dimensionless salt concentration, $\tilde{c}/\tilde{c}_0$ |
| $\tilde{c}$ | salt concentration in solution |
| $\tilde{c}_0$ | salt concentration in the bulk solution far from the patch |
| $\tilde{c}_i$ | concentration of ion $i$ in solution |
| $D_i$ | ion diffusion coefficient in solution |
| $E_0$ | constant bulk electric field |
| $f(s)$ | integration function in $G(x,y)$, see Eq. (16) |
| $F$ | Faraday's constant |
| $F(s)$ | generating function used in solving the concentration profile, Eqs. (23) and (24) |
| $G(x,y)$ | function that solves the Laplace equation, see Eq. (16) |
| $g_0(x,y)$ function for solving concentration profiles, see Eq. (26) | |
| $g_n(x,y)$ functions used to obtain the concentration profiles, see Eq. (57) | |
| $h(x,y)$ | function in Eq. (44) |
| $\vec{j}_i$ | vector flux of ion $i$ |
| $\vec{j}_1$ | counter ion vector flux |
| $\vec{j}_2$ | co-ion vector flux |
| $K(s)$ | nonlinear-correction function, see Eq. (52) |
| $l$ | half-width of the ion-exchange patch |
| $Q_n$ | moment of a multipole in the multipole approximation, Eq. (50) |
| $r$ | polar coordinate, Eq. (47) |
| $R$ | gas constant |
| $R_p(x,y)$ function defined for convenience in Eq. (62) | |
| $R_m(x,y)$ function defined for convenience in Eq. (63) | |
| $s$ | integration dummy variable |
| $s'$ | integration dummy variable |
| $T$ | temperature |
| $x$ | horizontal coordinate divide by the patch half width, $l$ |
| $x'$ | integration dummy variable |
| $y$ | vertical coordinate divide by the patch half width, $l$ |
| $y'$ | integration dummy variable |
| $Z_i$ | charge of ion $i$ |
| $Z_1$ | counter ion charge |
| $Z_2$ | co-ion charge |
| $\gamma_i$ | activity coefficient of ion $i$ |
| $\delta c$ | concentration perturbation, $c-1$ |
| $\delta\bar{\mu}_2$ | perturbation of the co-ion electrochemical potential |
| $\delta\bar{\mu}_2^{(2)}$ | second-order correction to the perturbation of co-ion electrochemical potential |
| $\theta$ | angle in polar coordinates, Eq. (48) |
| $\lambda$ | $\frac{FE_0 l}{2RT}$ dimensionless voltage drop on the quarter width of the ion-exchange patch |
| $\mu_i^\circ$ | standard state chemical potential of ion $i$ |
| $\bar{\mu}_1$ | counter ion electrochemical potential |
| $\bar{\mu}_2$ | co-ion electrochemical potential |
| $\nu_i$ | stoichiometric coefficient of ion $i$ in a salt |
| $\varphi$ | dimensionless electrostatic potential in solution (potential, $\tilde{\varphi}$, multiplied by F/RT) |
| $\tilde{\varphi}$ | electrostatic potential in solution |

## Acknowledgements

*We gratefully acknowledge funding of this work by the Division of Chemical Sciences, Geosciences, and Biosciences, Office of Basic Energy Sciences of the U.S. Department of Energy through Grant DE-SC0017618. A.Y. acknowledges funding from the Spanish Ministry of Economy and Competitiveness through project CTM2017-85346-R.*

**Keywords:** concentration polarization · electrophoresis · ion exchange · microfluidics · preconcentration

[1] J. Dai, T. Ito, L. Sun, R. M. Crooks, *J. Am. Chem. Soc.* **2003**, *125*, 13026–13027.
[2] F. Helfferich, *Ion Exch.*, McGraw-Hill, New York, NY, **1962**.
[3] R. Abu-Rjal, V. Chinaryan, M. Z. Bazant, I. Rubinstein, B. Zaltzman, *Phys. Rev. E* **2014**, *89*, 012302.
[4] R. Gloukhovski, V. Freger, Y. Tsur, *Reviews in Chemical Engineering* **2018**, *34*, 455.
[5] J. Ran, L. Wu, Y. He, Z. Yang, Y. Wang, C. Jiang, L. Ge, E. Bakangura, T. Xu, *J. Membr. Sci.* **2017**, *522*, 267–291.
[6] Z. Slouka, S. Senapati, H.-C. Chang, *Ann. Rev. Anal. Chem.* **2014**, *7*, 317–335.
[7] T. A. Zangle, A. Mani, J. G. Santiago, *Chem. Soc. Rev.* **2010**, *39*, 1014–1035.
[8] H. Chun, T. D. Chung, J. M. Ramsey, *Anal. Chem.* **2010**, *82*, 6287–6292.
[9] S. Marczak, K. Richards, Z. Ramshani, E. Smith, S. Senapati, R. Hill, D. B. Go, H.-C. Chang, *Electrophoresis* **2018**, *39*, 2029–2038.
[10] Y.-C. Wang, A. L. Stevens, J. Han, *Anal. Chem.* **2005**, *77*, 4293–4299.
[11] M. P. Bondarenko, M. L. Bruening, A. Yaroshchuk, *Adv. Theory & Sim.* **2019**, *2*, 1900009.
[12] F. Mavré, R. K. Anand, D. R. Laws, K.-F. Chow, B.-Y. Chang, J. A. Crooks, R. M. Crooks, *Anal. Chem.* **2010**, *82*, 8766–8774.
[13] W. Zhan, J. Alvarez, R. M. Crooks, *J. Am. Chem. Soc.* **2002**, *124*, 13265–13270.

[14] D. R. Laws, D. Hlushkou, R. K. Perdue, U. Tallarek, R. M. Crooks, *Anal. Chem.* **2009**, *81*, 8923–8929.
[15] R. K. Perdue, D. R. Laws, D. Hlushkou, U. Tallarek, R. M. Crooks, *Anal. Chem.* **2009**, *81*, 10149–10155.
[16] I. Dumitrescu, R. K. Anand, S. E. Fosdick, R. M. Crooks, *J. Am. Chem. Soc.* **2011**, *133*, 4687–4689.
[17] R. Dhopeshwarkar, D. Hlushkou, M. Nguyen, U. Tallarek, R. M. Crooks, *J. Am. Chem. Soc.* **2008**, *130*, 10480–10481.
[18] D. Hlushkou, R. K. Perdue, R. Dhopeshwarkar, R. M. Crooks, U. Tallarek, *Lab Chip* **2009**, *9*, 1903–1913.
[19] S. H. Ko, Y.-A. Song, S. J. Kim, M. Kim, J. Han, K. H. Kang, *Lab Chip* **2012**, *12*, 4472–4482.
[20] R.-J. Yang, H.-H. Pu, H.-L. Wang, *Biomicrofluidics* **2015**, *9*, 014122.
[21] S. H. Yeh, K. H. Chou, R. J. Yang, *Lab Chip* **2016**, *16*, 925–931.
[22] S. I. Han, Y. K. Yoo, J. Lee, C. Kim, K. Lee, T. H. Lee, H. Kim, D. S. Yoon, K. S. Hwang, R. Kwak, J. H. Lee, *Sens. Actuators B* **2018**, *268*, 485–493.
[23] Y. Ji, H. Luo, G. M. Geise, *J. Membr. Sci.* **2018**, *563*, 492–504.
[24] M. Jia, T. Kim, *Anal. Chem.* **2014**, *86*, 7360–7367.
[25] W. Ouyang, X. H. Ye, Z. R. Li, J. Hang, *Nanoscale* **2018**, *10*, 15187–15194.
[26] M. Shen, H. Yang, V. Sivagnanam, M. A. M. Gijs, *Anal. Chem.* **2010**, *82*, 9989–9997.
[27] L. Rosentsvit, S. Park, G. Yossifon, *Phys. Rev. E* **2017**, *96*, 7.
[28] A. Yaroshchuk, M. Bondarenko, C. Tang, M. L. Bruening, *Langmuir* **2019**.

Manuscript received: December 13, 2019
Revised manuscript received: February 3, 2020

# ARTICLES

**Time to concentrate:** Applied electric fields in channels containing ion-exchange patches lead to depletion of salt near the patch entrance and accumulation near the exit, which may enable preconcentration of trace co-ions. This work mathematically investigates this salt concentration polarization and develops methods for expressing concentration profiles with a simple 4x7 coefficient matrix.

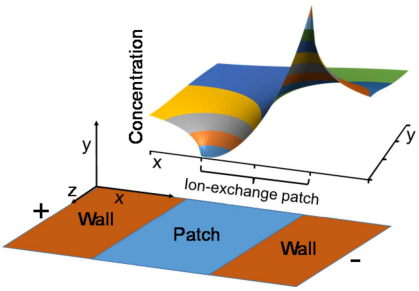




## SPACE RESERVED FOR IMAGE AND LINK

Share your work on social media! *ChemElectroChem* has added Twitter as a means to promote your article. Twitter is an online microblogging service that enables its users to send and read short messages and media, known as tweets. Please check the pre-written tweet in the galley proofs for accuracy. If you, your team, or institution have a Twitter account, please include its handle @username. Please use hashtags only for the most important keywords, such as #catalysis, #nanoparticles, or #proteindesign. The ToC picture and a link to your article will be added automatically, so the **tweet text must not exceed 250 characters**. This tweet will be posted on the journal's Twitter account (follow us @ChemElectroChem) upon publication of your article in its final (possibly unpaginated) form. We recommend you to re-tweet it to alert more researchers about your publication, or to point it out to your institution's social media team.

### ORCID (Open Researcher and Contributor ID)

Please check that the ORCID identifiers listed below are correct. We encourage all authors to provide an ORCID identifier for each coauthor. ORCID is a registry that provides researchers with a unique digital identifier. Some funding agencies recommend or even require the inclusion of ORCID IDs in all published articles, and authors should consult their funding agency guidelines for details. Registration is easy and free; for further information, see http://orcid.org/.

Prof. Mykola P. Bondarenko
Prof. Merlin L. Bruening http://orcid.org/0000-0002-4553-5143
Prof. Andriy E. Yaroshchuk